SCIENTIFIC REPORTS

OPEN

Self-reference and random sampling approach for label-free identification of DNA composition using plasmonic nanomaterials

Received: 25 October 2017
Accepted: 17 April 2018
Published online: 09 May 2018

Lindsay M. Freeman, Lin Pang & Yeshaiahu Fainman

The analysis of DNA has led to revolutionary advancements in the fields of medical diagnostics, genomics, prenatal screening, and forensic science, with the global DNA testing market expected to reach revenues of USD 10.04 billion per year by 2020. However, the current methods for DNA analysis remain dependent on the necessity for fluorophores or conjugated proteins, leading to high costs associated with consumable materials and manual labor. Here, we demonstrate a potential label-free DNA composition detection method using surface-enhanced Raman spectroscopy (SERS) in which we identify the composition of cytosine and adenine within single strands of DNA. This approach depends on the fact that there is one phosphate backbone per nucleotide, which we use as a reference to compensate for systematic measurement variations. We utilize plasmonic nanomaterials with random Raman sampling to perform label-free detection of the nucleotide composition within DNA strands, generating a calibration curve from standard samples of DNA and demonstrating the capability of resolving the nucleotide composition. The work represents an innovative way for detection of the DNA composition within DNA strands without the necessity of attached labels, offering a highly sensitive and reproducible method that factors in random sampling to minimize error.

The evaluation of DNA without costly DNA sequencing[1,2] or labeling methods[3] is imperative to reducing healthcare costs, so efforts must be made to develop DNA screening technologies that rely on cost reduction technology and scientific simplicity. Here, we examine a new label-free DNA detection method using surface-enhanced Raman spectroscopy (SERS)[4–6], an optical technique that probes molecules directly rather than relying on the use of labels. SERS has been proposed as a label-free detection method of DNA[7–9] due to the rich molecular information that Raman scattering reveals[10–14], but previous attempts have suffered from the inability to quantify information related to the composition of DNA[12,15]. We report an approach to accurately identify the composition of the DNA bases adenine and cytosine benefiting from the fact that each base shares the same phosphate backbone structure, which can be treated as a reference to extract the base composition of adenine and cytosine within the DNA strands. This self-reference approach would be immune to varying experimental conditions due to the normalization of the data, as compared to other experiments that rely on absolute intensity measurements in which the signal varies as conditions change.

The self-reference approach provides a calculated ratio of the nucleotide signal with respect to the phosphate backbone, regardless of the variation in experimental conditions. Additionally, a highly accurate and precise statistical distribution can be maintained when a large number of experiments are conducted with uncontrollable environmental conditions via random sampling, which combined with the self-reference approach can be employed to determine the nucleotide composition in the DNA strand. As an example, we employ SERS as a demonstration of the self-reference approach, in which the nucleotide composition is acquired from several samples of synthesized DNA strands composed of varying mixtures of adenine and cytosine. In this case, a high concentration of adenine and cytosine is used in order to maximize the SERS signal at short acquisition times. Additionally, as this is the first demonstration of this technique, we selected adenine and cytosine due to the fact that their prominent Raman modes do not overlap with each other or the phosphate backbone mode, and thus are

Department of Electrical and Computer Engineering, University of California San Diego, 9500 Gilman Drive, La Jolla, California, 92093-0407, USA. Correspondence and requests for materials should be addressed to Y.F. (email: fainman@eng.ucsd.edu)

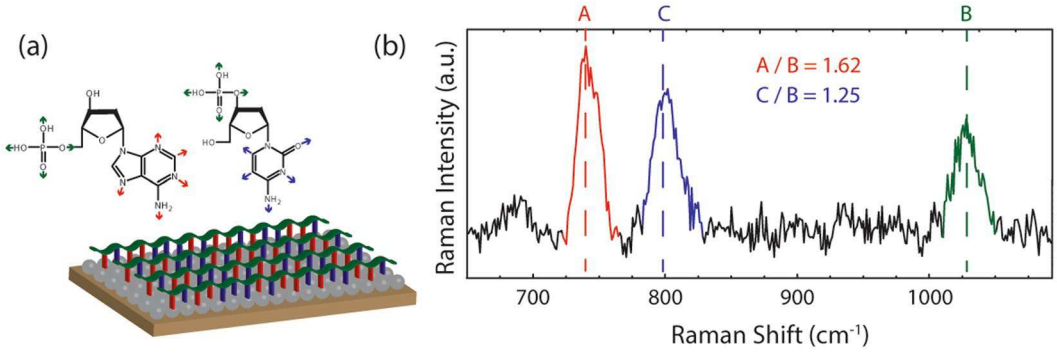

Figure 1. Normalization procedure for DNA composition detection using Raman spectroscopy. (**a**) Illustration of ssDNA functionalized to random silver films on mica showing the ring-breathing-modes of adenine (red), cytosine (blue) and the phosphate backbone mode of DNA (green). (**b**) Proposed normalization procedure in which the intensity of the adenine ring-breathing-mode (508 a.u.), of the cytosine ring-breathing-mode (394 a.u.), and of the backbone mode (314 a.u.) are used to calculate the A/B ratio (1.62) and C/B ratio (1.25).

the ideal bases to utilize as a proof of concept. Future studies will take into account the additional bases of guanine and thymine; however, as a preliminary demonstration, only adenine and cytosine were analyzed in this work.

To demonstrate the simplicity of a self-reference approach on readily available substrates, we employ low cost random silver films as plasmonic resonators that localize the electromagnetic field for improved optical signal generation[16–19]. The self-reference of the phosphate backbone provides statistical bias to eliminate the nature of the experimental variation, which in our case, is caused by the DNA orientation on the metal surface, random distribution of plasmonic particles, and variable signal to noise ratio. The random silver films used in this work are fabricated in an uncontrolled manner, and thus have an uneven distribution of plasmonic hot-spots. However, as demonstrated in this work, the variation in the electromagnetic field enhancement is significantly reduced by taking into account hundreds of Raman spectra that minimize the input noise into our system.

Because measured SERS spectra vary across similar samples of interest and thus offer poor quantitative information, based on the self-reference strategy discussed above, we introduce a normalization procedure in which the ratio of the ring-breathing-modes of the nucleotides to the backbone mode of the DNA is found for each spectrum. When measuring various compositions of nucleotides within DNA strands using SERS, the number of each nucleotide will vary while the amount of DNA backbone will remain constant (Fig. 1a). Thus, the normalization procedure is dependent on the backbone mode as it stays constant throughout the spectral measurements. As shown in Fig. 1b, the strong Raman spectral features of the ssDNA are the ring-breathing-modes for adenine (735 cm^{-1}) and cytosine (795 cm^{-1}) and the phosphate backbone mode of the DNA strand (1030 cm^{-1}). The intensity counts for each mode are used to calculate the A/B and C/B ratios and is the standard metric used to compare different compositions of DNA strands. The current work demonstrates the feasibility of a self-reference approach for the identification of nucleotide composition within DNA using a simplified model, in which synthesized single strands of DNA composed of adenine and cytosine are functionalized to random silver films and the SERS spectra are acquired.

Results

There are significant variations in the detected Raman signals across the same sample, which can be attributed to disproportionate distributions of hot spots, inconsistent functionalization of DNA strands, and fluctuations in optical setup. Here, we aim to use random sampling in surface-enhanced Raman spectroscopy to collect sufficient Raman data that provides an accurate representation of the sample population to make appropriate inferences regarding the composition within DNA strands. Thus, we use random silver films as the SERS substrates, as the substrates produce nanoscale islands that generate localized electromagnetic field enhancement while also providing a random distribution of hot-spots that limits systematic bias. We perform a Raman mapping procedure, in which we measure 400 Raman spectra across an area of approximately 100 by 100 microns of ssDNA containing 150 bases of adenine and 50 bases of cytosine (75% A/25% C) functionalized to the random silver films (Fig. 2a, methods). When qualitatively and quantitatively analyzing the data, it is apparent that there are fluctuations between each individual Raman spectrum due to the random hotspot distribution and variations in the ssDNA functionalization. As shown in Fig. 2b, five sample Raman spectra from the 75% A/25% C ssDNA show differences in the A/B and C/B ratios between each spectrum despite being acquired from the same scan. Thus, relying on a limited number of Raman spectra to extract quantitative information from the system is insufficient for the calculation of nucleic acid composition within DNA strands. Instead, we use the entire 400 Raman measurement set to accurately represent the system under study. To obtain an accurate representation of the population, we calculate the normalization ratio for each Raman spectrum in the set of 400, and then plot the probability density function (PDF) of the normalization ratio based on the 400 measurements. As an example, the probability density function of A/B ratio for the 75% A/25% C sample is shown in Fig. 2c, in which a lognormal distribution (red) is shown to be a best fit. To confirm the appropriateness of the lognormal distribution fit, we plot the cumulative density function (Fig. 2d) and the theoretical vs. empirical probabilities (Fig. 2e), which visually show the goodness of fit of the lognormal distribution for the probability distribution of the normalization ratio.

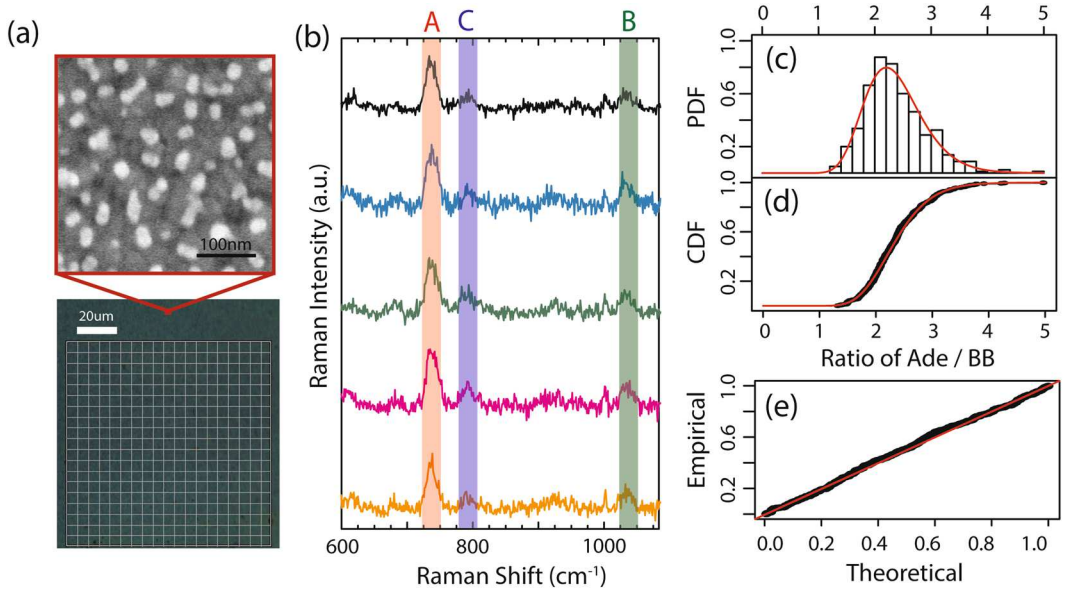

Figure 2. Random Raman mapping of ssDNA funtionalized to silver films. (**a**) Scanning electron microscope image of random silver films grown on mica and bright field image of ssDNA functionalized to random silver films on mica with the outline of the Raman map, in which 400 measurements are acquired in an approximately 100 micron by 100 micron area. (**b**) Example Raman spectra for 5 measurements of 75% A/25% C ssDNA mixture functionalized to random silver films, with the adenine ring-breathing-mode (red, 735 cm^{-1}), cytosine ring-breathing-mode (blue, 795 cm^{-1}), and backbone mode (green, 1035 cm^{-1}) labeled. (**c**) Probability density function (PDF) of the A/B ratio for the 75% A/25% C mixture, showing the best fit lognormal distribution with a lognormal median at A/B = 2.36. (**d**) Cumulative distribution function (CDF) of the 400 Raman measurements (black), with the calculated lognormal distribution (red). (**e**) Probability-probability plot visually demonstrating the goodness of fit with a lognormal distribution.

After establishing the necessary constraints to account for variations and fluctuations across samples, we propose to measure the composition within a random strand of DNA by first establishing a calibration curve using several known standards of DNA mixtures. To measure the composition of nucleic acids, ssDNA of 200 bases in length were purchased from Integrated DNA Technologies with the following compositions: (1) 200 bases of cytosine (0% A, 100% C), (2) 50 bases of adenine and 150 bases of cytosine (25% A/75% C), (3) 100 bases of adenine and 100 bases of cytosine (50% A/50% C), (4) 150 bases of adenine and 50 bases of cytosine (75% A/25% C), and (5) 200 bases of adenine (100% A, 0% C), (sequences found in Table S1).

To generate the calibration curve for the estimation of composition within DNA using the random Raman sampling procedure, we perform 400 measurements on each standard and plot the probability density functions for each standard. A single Raman spectrum for each standard is shown in Fig. 3a, in which the A/B and C/B ratios are dependent on the composition of the corresponding nucleotide in the ssDNA. The PDFs for the ratios of A/B and C/B (Fig. 3b) for each standard demonstrate that the ratios for each standard follow lognormal distributions, as seen previously with the example of A/B ratio of 75% A/25% C standard in Fig. 2c–e. Incorporating 400 measurements and calculating the lognormal distribution provides more accurate information related to the composition of nucleotides in DNA strands in comparison to relying on single measurements, and thus more precise calibration curves can be generated from the Raman measurements.

To reduce the error in the calibration curve, two 400 Raman mapping procedures are performed for each standard with a total of 10 points (median of each lognormal distribution) used for the calibration curve. The summary of the medians of the lognormal distributions can be found in Table 1, in which it is apparent that the ratio of adenine to the backbone mode increases exponentially with respect to composition while the ratio of cytosine to the backbone mode increases linearly with respect to composition. The nonlinear dependence of the adenine normalization ratio is caused by the charge-transfer effect that generates a stronger chemical resonance[20] with a higher composition of adenine molecules at a Raman excitation wavelength of 785 nm. The linear dependence of the cytosine normalization ratio is due to the lack of charge-transfer effect at 785 nm[21]; though it is important to note that at shorter wavelengths (e.g. 532 nm) the cytosine normalization ratio will have a nonlinear dependence. The calibration curves for both adenine and cytosine can be found in Fig. 4b, with best fit equations of $\ln(R_A) = 0.0278\ C_A - 1.25$ and $R_C = 0.0140\ C_C + 0.567$ and coefficient of determinations of $r_A = 0.997$ and $r_C = 0.994$, respectively (S4). The non-zero y-intercept is caused by the positive peak intensities between the ranges of 725 cm^{-1} and 750 cm^{-1} for adenine and 785 cm^{-1} and 810 cm^{-1} for cytosine. For adenine, the positive peak intensity is attributed to noise, while for cytosine, the positive peak intensity is caused by both noise and the existence of the phosphate skeleton stretching Raman mode of DNA which overlaps with the cytosine ring-breathing-mode. A discussion and example spectrum demonstrating the cause of the non-zero y-intercepts can be found in S2. The limits of detection (LOD) can be calculated by $LOD = 3.3\frac{S_y}{m}$ where Sy is the standard

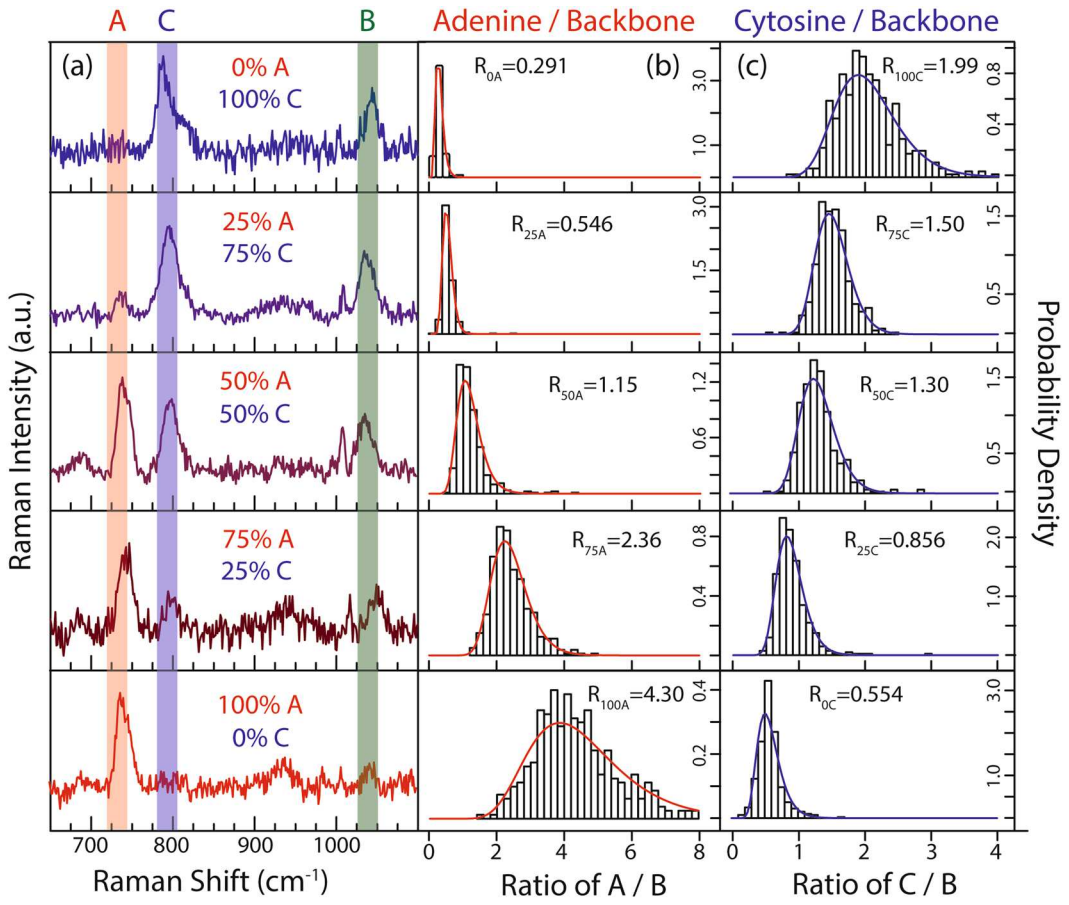

Figure 3. Raman spectra and corresponding probability distributions for the 5 standards. (**a**) Example Raman spectrum for each calibration standard with the adenine ring-breathing-mode (red), cytosine ring-breathing-mode (blue), and backbone mode (green) contained in the vertical shaded rectangle (see S2 for mode selection). (**b**) and (**c**) Probability density functions for the normalized ratios (A/B and C/B) for the 5 standards, showing the median of the lognormal distributions (R).

Measurement	Lognormal Median of A/B	Lognormal Median of C/B
0% A/100% C #1	0.291	1.99
0% A/100% C #2	0.250	1.94
25% A/75% C #1	0.546	1.50
25% A/75% C #2	0.598	1.61
50% A/50% C #1	1.15	1.30
50% A/50% C #2	1.14	1.31
75% A/25% C #1	2.36	0.856
75% A/25% C #2	2.41	0.864
100% A/0% C #1	4.30	0.554
100% A/0% C #2	4.49	0.635
Random Sample #1	0.968	1.37
Random Sample #2	0.922	1.35
Random Sample #3	0.959	1.36

Table 1. Median of the lognormal distributions for each standard and the random sample.

deviation of the response and m is the slope of the calibration curve. Thus, the LOD for adenine and cytosine are compositions of 9.32% and 13.0%, respectively. To determine the composition of a random strand of DNA, we used a randomization algorithm to generate a random sequence of DNA containing 200 bases of both adenine and cytosine. The resulting ssDNA was purchased from Integrated DNA Technologies and contained 45% A and 55% C (sequence in Table S1). Three 400 Raman mapping procedures are performed on the random sample of

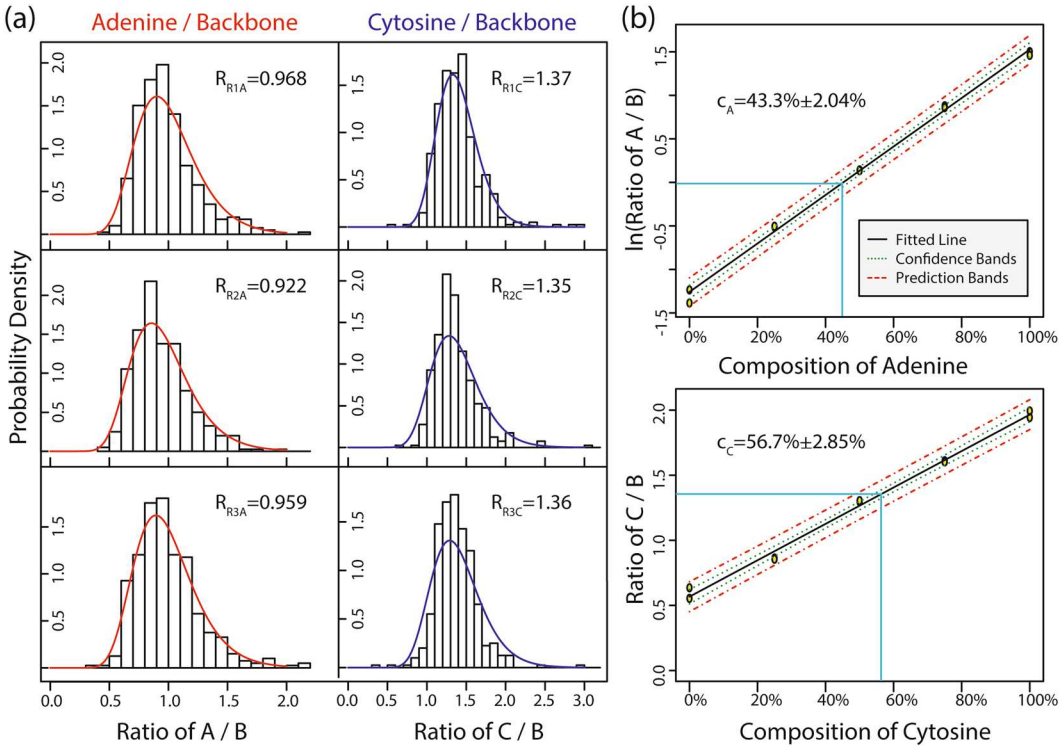

Figure 4. Probability density functions and calibration curve for detection of composition within random ssDNA. (**a**) PDFs of 3 sets of measurements on a random composition of ssDNA with the corresponding lognormal median of each measurement (R). (**b**) Calibration curve based on 2 sets of measurements from each standard (10 total) and the corresponding identification of the composition using the average normalization ratios of the 3 random samples.

DNA and the PDFs are calculated (Fig. 4a). Using the best fit equations, the compositions of A and C are determined to be $C_A = 43.3\% \pm 2.04\%$ and $C_C = 56.7\% \pm 2.85\%$, respectively.

Discussion

Here, we have shown the feasibility of calculating the composition of DNA strands with a standard error of ± 2.04% and ± 2.85% for A and C, respectively, using cost efficient random silver films and a low concentration of DNA. To qualitatively compare this technique to a random Raman mapping procedure without SERS, we functionalized the ssDNA to mica and acquired the normal Raman scattering (NRS) spectra which results in a poor signal to noise ratio and greater variance in the A/B and C/B ratios. Using the 50% A/50% C standard, the average peak intensities of the A and C ring-breathing-modes for the normal Raman scattering spectra set are measured at 71.9 a.u. and 73.4 a.u., respectively. This is lower than the average peak intensities of the A and C ring-breathing-modes for the SERS spectra set, which are 468 a.u. and 510 a.u., respectively. Thus, the surface-enhanced affect improves the signal to noise ratio and also reduces the variation in the measured signals, allowing for a lower standard error in the calibration curves. To visualize this difference, Fig. 5 shows the population distributions with the fitted lognormal probability density functions for the A/B and C/B ratios of the normal Raman scattering (NRS) spectra set and the surface-enhanced Raman scattering (SERS) spectra set. The larger variances of NRS (1.05 for A/B and 0.847 for C/B) compared to the variances of SERS (0.428 for A/B and 0.340 for C/B) suggest that the standard error for NRS will be much greater than that of SERS. This also suggests that incorporating a SERS substrate with a greater enhancement will reduce the variance and minimize the standard error.

Thus, we have demonstrated that our method is a great improvement over performing these measurements using normal Raman scattering without enhancement from a SERS substrate. To further improve our method to achieve single nucleotide resolution in the future, we propose to implement high local field enhancement factor nanoplasmonic resonators[22–24] that will greatly enhance the signal to noise ratio of the system. Despite the cost efficiency of random silver films, they are poor SERS substrates due to their weak local field enhancement with LFE estimations between 0.9 to 2.5, depending on fill factor and excitation wavelength[25]. We can aim for the utilization of resonators capable of highly confining the local electric field, which will increase the LFE from a maximum of 2.5 to a range of 10–100[26,27]. Using plasmonic resonators capable of LFE between 10 to 100 would drastically increase the signal to noise ratio, which in turn would reduce our standard error to a level capable of achieving single nucleotide resolution.

In this work, we demonstrated label-free detection of the adenine and cytosine composition within DNA strands using a random Raman mapping procedure. Single strands of DNA composed of adenine and cytosine were functionalized to random silver films, and 400 Raman measurements were acquired for 5 different

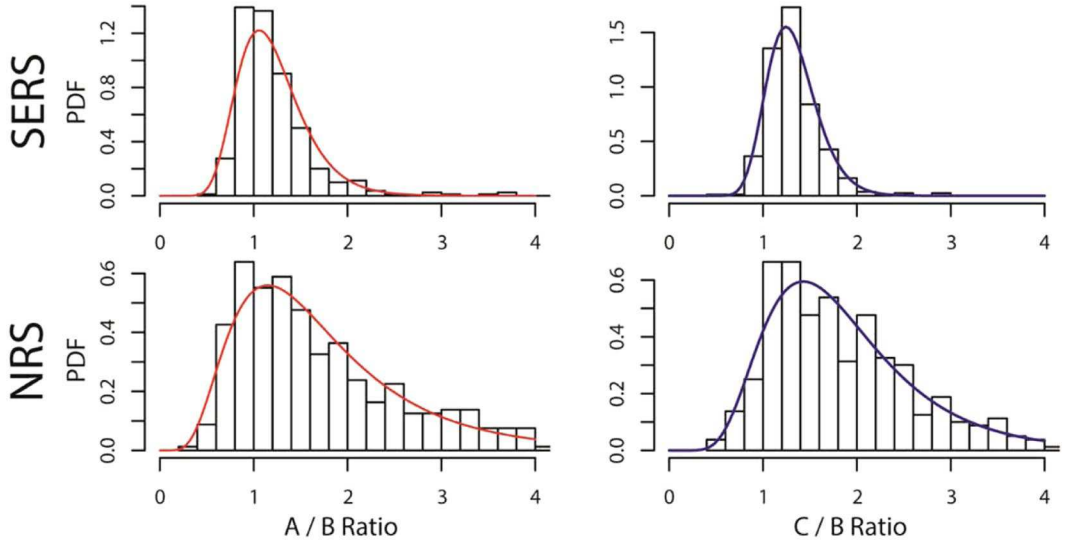

Figure 5. Comparison of SERS and NRS for the 50% A/50% C standard, showing a tighter distribution for the SERS sample.

standards. The normalization ratio of the adenine and cytosine to backbone modes were calculated for each set of measurements, and the probability density functions were calculated which fit lognormal distributions. Calibration curves were generated using the standards, and the nucleotide composition of a random sequence of ssDNA was estimated. Thus, this work shows promise in implementing this novel method as a technique in determining the composition of bases within DNA strands without the use of labels.

While the work discussed here is promising, additional method development is necessary to realize eventual application for DNA composition detection. This work focused on adenine and cytosine as a proof of concept, so future direction will consist of determining the composition of all bases within random strands of DNA. This may present some technical challenges as the thymine ring-breathing-mode at ~800 cm^{-1} overlaps with the cytosine ring-breathing-mode at 795 cm^{-1}, so the signals must be deconvoluted from each other. Additional future developments will incorporate higher local field enhancement nanoplasmonic resonators that will increase the signal to noise ratio, reduce variation in the Raman spectra, and minimize standard error in the calibration curve. Eventually, the aim of the technique is to utilize this method for future label-free studies of DNA, in which distinctions can be made on changes to the DNA composition without the need to modify the DNA using standard techniques such as labeling assays.

Methods

For the experimental measurements, silver films are fabricated by depositing 300 Å of silver using an e-beam evaporator (Temescal BJD, UCSD Nano3 Cleanroom) on a mica substrate. To functionalize the ssDNA to the random silver films, ssDNA solutions were prepared by diluting the DNA stock solution to 50 ng/uL in HEPES and then forming a 1:1 mixture of the ssDNA solution to 10 mM magnesium chloride. A table of the sequences for each ssDNA standard can be found in the supplementary information. The DNA concentration selected was chosen to ensure sufficient coverage, and the corresponding salt ratio was used to neutralize the phosphate backbone and promote attachment of the nucleotides directly to the silver. 20 uL of each solution was deposited onto separate substrates of random silver films for 25 minutes, followed by rinsing with buffer and drying under nitrogen gas to remove multilayers of DNA.

Raman spectra were acquired using a Renishaw inVia Raman spectrometer, using a 785 nm 500 mW continuous wave laser at a power of 1% and an acquisition time of 3 s. The grating was set to static with a spectrum range of ~100 cm^{-1} to 1100 cm^{-1} for each measurement. The Raman mapping feature was used to acquire 400 measurements in a 20 × 20 unit area, with each unit representing an area of ~ 25 μm^2. After acquiring the 400 measurements, cosmic ray removal and baseline subtraction using the Intelligent Fitting function were performed using the Renishaw WiRE 4.2 software. MATLAB was used to find the peak intensity for the ring-breathing-modes of adenine (between 725 cm^{-1} and 750 cm^{-1}) and cytosine (between 785 cm^{-1} and 810 cm^{-1}) and the phosphate backbone mode of DNA (between 1020 cm^{-1} and 1045 cm^{-1}) for each of the 400 spectra. The A/B and C/B histograms of the 400 measurements was plotted in R, and the lognormal distribution fit parameters were calculated using the fitdistrplus package. Additional information on the fitting models can be found in the supplementary information.

References

1. Shendure, J. & Ji, H. Next-generation DNA sequencing. *Nat. Biotechnol.* **26**, 1135–45 (2008).
2. Branton, D. *et al*. The potential and challenges of nanopore sequencing. *Nat. Biotechnol.* **26**, 1146–53 (2008).
3. Mitra, R. D., Shendure, J., Olejnik, J., Edyta-Krzymanska-Olejnik & Church, G. M. Fluorescent *in situ* sequencing on polymerase colonies. *Anal. Biochem.* **320**, 55–65 (2003).

4. Albrecht, M. G. & Creighton, J. A. Anomalously intense Raman spectra of pyridine at a silver electrode. *J. Am. Chem. Soc.* **99**, 5215–5217 (1977).
5. Jeanmaire, D. L. & Van Duyne, R. P. Surface raman spectroelectrochemistry. *J. Electroanal. Chem. Interfacial Electrochem.* **84**, 1–20 (1977).
6. King, F. W., Van Duyne, R. P. & Schatz, G. C. Theory of Raman scattering by molecules adsorbed on electrode surfaces. *J. Chem. Phys.* **69**, 4472 (1978).
7. Bell, S. E. J. & Sirimuthu, N. M. S. Surface-Enhanced Raman Spectroscopy (SERS) for Sub-Micromolar Detection of DNA/RNA Mononucleotides. (2006).
8. Papadopoulou, E. & Bell, S. E. J. Label-Free Detection of Single-Base Mismatches in DNA by Surface-Enhanced Raman Spectroscopy. *Angew. Chemie Int. Ed* **50**, 9058–9061 (2011).
9. Barhoumi, A. & Halas, N. J. Label-Free Detection of DNA Hybridization Using Surface Enhanced Raman Spectroscopy. *J. Am. Chem. Soc.* **132**, 12792–12793 (2010).
10. Wachsmann-Hogiu, S., Weeks, T. & Huser, T. Chemical analysis *in vivo* and *in vitro* by Raman spectroscopy–from single cells to humans. *Curr. Opin. Biotechnol.* **20**, 63–73 (2009).
11. Campion, A. & Kambhampati, P. Surface-enhanced Raman scattering. *Chem. Soc. Rev.* **27**, 241 (1998).
12. Bantz, K. C. *et al*. Recent progress in SERS biosensing. *Phys. Chem. Chem. Phys.* **13**, 11551–67 (2011).
13. Raman, C. V. A Change of Wave-length in Light Scattering. *Nature* **121**, 619–619 (1928).
14. Raman, C. V. & Krishnan, K. S. A New Type of Secondary Radiation. *Nature* **121**, 501–502 (1928).
15. Gao, F., Lei, J. & Ju, H. Label-Free Surface-Enhanced Raman Spectroscopy for Sensitive DNA Detection by DNA-Mediated Silver Nanoparticle Growth. *Anal. Chem.* **85**, 11788–11793 (2013).
16. Kelly, K. L., Coronado, E., Zhao, L. L. & Schatz, G. C. The Optical Properties of Metal Nanoparticles: The Influence of Size, Shape, and Dielectric Environment. *J. Phys. Chem. B* **107**, 668–677 (2003).
17. Mulvihill, M. J., Ling, X. Y., Henzie, J. & Yang, P. Anisotropic Etching of Silver Nanoparticles for Plasmonic Structures Capable of Single-Particle SERS. 895–901 (2010).
18. Jain, P. K., Huang, X., El-Sayed, I. H. & El-Sayed, M. A. Review of Some Interesting Surface Plasmon Resonance-enhanced Properties of Noble Metal Nanoparticles and Their Applications to Biosystems. *Plasmonics* **2**, 107–118 (2007).
19. Dadosh, T. Synthesis of uniform silver nanoparticles with a controllable size. *Mater. Lett.* **63**, 2236–2238 (2009).
20. Myers, A. B. Resonance Raman Intensities and Charge-Transfer Reorganization Energies. (1996).
21. Freeman, L. M., Pang, L. & Fainman, Y. Maximizing the electromagnetic and chemical resonances of surface-enhanced Raman scattering for nucleic acids. *ACS Nano* **8**, 8383–91 (2014).
22. Liu, H. *et al*. Single molecule detection from a large-scale SERS-active $Au_{79}Ag_{21}$ substrate. *Sci. Rep* **1**, 112 (2011).
23. Graham, D., Thompson, D. G., Smith, W. E. & Faulds, K. Control of enhanced Raman scattering using a DNA-based assembly process of dye-coded nanoparticles. *Nat. Nanotechnol.* **3**, 548–51 (2008).
24. Su, K.-H. *et al*. Raman enhancement factor of a single tunable nanoplasmonic resonator. *J. Phys. Chem. B* **110**, 3964–8 (2006).
25. Karbovnyk, I. *et al*. Random nanostructured metallic films for environmental monitoring and optical sensing: experimental and computational studies. *Nanoscale Res. Lett.* **10**, 151 (2015).
26. Smolyaninov, A., Pang, L., Freeman, L., Abashin, M. & Fainman, Y. Broadband metacoaxial nanoantenna for metasurface and sensing applications. *Opt. Express* **22**, 22786–93 (2014).
27. Zhang, Q., Large, N., Nordlander, P. & Wang, H. Porous Au Nanoparticles with Tunable Plasmon Resonances and Intense Field Enhancements for Single-Particle SERS. *J. Phys. Chem. Lett.* **5**, 370–374 (2014).

Acknowledgements

This work was supported by the National Science Foundation (NSF) (CBET-1704085), the Office of Naval Research Multidisciplinary Research Initiative (N00014-13-1-0678), the NSF (DMR-1707641, ECCS-1405234, ECCS-1507146, and CCF-1640227), the NSF Center for Integrated Access Networks (EEC-0812072, Sub 502629), the Defense Advanced Research Projects Agency (N66001-12-1-4205) and the Cymer Corporation. This work was performed in part at the San Diego Nanotechnology Infrastructure (SDNI) of UCSD, a member of the National Nanotechnology Coordinated Infrastructure, which is supported by the National Science Foundation (Grant ECCS-1542148). A description of the methods, table of the ssDNA sequences, lognormal distribution plots for additional measurements, and statistical calculations are available in supporting information. This material is available free of charge via the Internet at http://pubs.acs.org.

Author Contributions

L.M.F. performed the experiments, analyzed the data, and co-wrote the manuscript. L.P. and Y.F. contributed to data interpretation and co-wrote the manuscript. All authors discussed the results and commented on the manuscript.

Additional Information

Supplementary information accompanies this paper at https://doi.org/10.1038/s41598-018-25444-2.

Competing Interests: The authors declare no competing interests.

Publisher's note: Springer Nature remains neutral with regard to jurisdictional claims in published maps and institutional affiliations.

Tribology Letters (2018) 66:54
https://doi.org/10.1007/s11249-018-1005-2

ORIGINAL PAPER

Tip-Enhanced Raman Spectroscopy Studies on Amorphous Carbon Films and Carbon Overcoats in Commercial Hard Disk Drives

Andreas Rosenkranz[1] · Lindsay Freeman[2] · Benjamin Suen[1] · Yeshaiahu Fainman[2] · Frank E. Talke[1]

Received: 14 January 2018 / Accepted: 21 February 2018

Abstract
Far-field Raman spectroscopy and tip-enhanced Raman spectroscopy were used to investigate 20-nm-thick amorphous carbon films and 3-nm-thick carbon overcoats of commercial hard disk drives. Enhancement of the Raman signal on both samples was observed indicating the activation of surface plasmons. The largest enhancement was found for the 3-nm-thick carbon overcoat of a commercial hard disk suggesting that the chemistry of nanometer-thick carbon films can be studied using tip-enhanced Raman spectroscopy with high sensitivity and resolution.

Keywords Hard disk drives · Carbon overcoats · Diamond-like carbon · Tip-enhanced Raman spectroscopy

1 Introduction

In the last decade, tip-enhanced Raman spectroscopy has been utilized for sensing and chemical imaging of materials and especially carbon materials on the nanoscale [1, 2]. In order to realize tip-enhanced Raman spectroscopy, a Raman spectrometer is coupled with either an atomic force microscope, a shear force microscope or a scanning tunneling microscope [3]. The laser light of the Raman spectrometer is focused on the metalized tip of any of those scanning devices. If the tip is in close proximity of the surface of interest, the metalized tip acts as an antenna for light, inducing surface plasmons and consequently enhancing the emitted electric field [4–6]. Due to the large field enhancement encountered, materials known to be weak Raman scatterers can be probed with high resolution. Hayazawa et al. investigated single-wall carbon nanotubes and amorphous carbon films by tip-enhanced Raman spectroscopy and compared the respective far-field spectra with the tip-enhanced signals. For single-wall carbon nanotubes, they demonstrated a selective enhancement of the G-peak, while amorphous carbon exhibited a more pronounced D-peak [7]. Chen et al. verified a spatial resolution of 1.7 nm using tip-enhanced Raman spectroscopy with a scanning tunneling microscope and individual carbon nanotubes as probed material. Local defects, bundling effects and different types of carbon nanotubes were imaged with high resolution. In addition, the authors showed a stronger enhancement of the G-peak compared to the D-peak [8]. Using a tip-enhanced Raman setup based upon a scanning tunneling microscope, Liao et al. could verify a spatial resolution of 0.7 nm for individual carbon nanotubes. The high resolution makes tracking of strain-induced structural changes possible. Bending experiments on individual carbon nanotubes and in situ tip-enhanced Raman spectroscopy measurements revealed a split up of the G-peak which depends on the degree of deformation [9]. Saito et al. studied the influence of the polarization of the exciting laser source on the resulting spectra of single-wall carbon nanotubes recorded by tip-enhanced Raman spectroscopy. The polarization was varied between s-polarization (parallel to the sample plane) and p-polarization (perpendicular to the sample plane). They observed a selective enhancement of the G-peak using s-polarized laser light, while p-polarized light enhances more the radial breathing mode. This selective enhancement of vibrational modes can be explained by the connection of the laser polarization and the orientation of vibrational moments on the molecular level. Comparing far- and near-field measurements, Saito et al. [10] observed a maximum enhancement factor of 2.5 for the G-peak. As demonstrated in the studies discussed above, tip-enhanced Raman spectroscopy is a powerful tool

✉ Andreas Rosenkranz
arosenkranz@ucsd.edu

[1] Center for Memory and Recording Research, UC San Diego, La Jolla, CA 92093, USA

[2] Electrical and Computer Engineering Department, UC San Diego, La Jolla, CA 92093, USA

Published online: 01 March 2018

for studying changes in structure and chemistry of carbon nanoparticles and/or nanometer-thick carbon films with high accuracy and sensitivity.

In this study, 20-nm-thick amorphous carbon films consisting of sp^2- and sp^3-hybridized carbon were investigated by tip-enhanced Raman spectroscopy. In addition, carbon overcoats used in hard disk drives with a film thickness of two to three nanometers were studied using tip-enhanced Raman spectroscopy. Our goal is to verify that tip-enhanced Raman spectroscopy can be used to characterize structural changes in nanometer-thick carbon films with mixed sp^2–sp^3-hybridization as used for carbon overcoats in commercial hard disk drives.

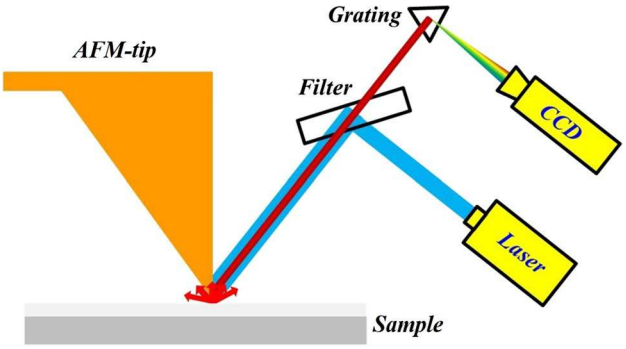

Fig. 1 Schematic illustration of the used tip-enhanced Raman spectroscopy system consisting of an atomic force microscope and a Raman spectrometer

2 Experimental

2.1 Plasma-enhanced Chemical Vapor Deposition

Amorphous carbon films with a thickness of 20 nm were deposited on a silicon wafer using the following procedure. First, the wafer was cleaned and stripped of its native oxide layer. The silicon wafers used in this experiment were metal-backed *p*-type < 100 > wafers. The native oxide layer was removed by dipping the wafer in a 2% hydrofluoric acid bath for 5 min, and a 20-nm-thick amorphous carbon film was deposited using plasma-enhanced chemical vapor deposition. The films were deposited on the polished bare silicon side of the wafer. An Oxford Plasmalab 80 was used as deposition tool. The amorphous carbon was deposited by decomposing methane at 100 mTorr pressure, 20 °C temperature and 50 standard cubic centimeters per minute flow rate using 250 W of RF power.

2.2 Commercial Hard Disk Drive

The hard disk drive media was cut from a 3.5-inch aluminum disk intended for use in production drives. The carbon overcoat on the media was about 2.5 nm thick and was fabricated by conventional sputtering techniques. The carbon overcoat is protected with a monolayer of perfluoropolyether-based lubricant of approximately 1.5 nm thickness.

2.3 Tip-Enhanced Raman Spectroscopy

Tip-enhanced Raman measurements were performed using confocal Raman spectrometer (Renishaw inVia) coupled with an atomic force microscope (Nanonics MV 2000), as schematically shown in Fig. 1.

A 532-nm excitation laser was used with acquisition time of 60 s. The optics within the Raman spectrometer consist of a 130 cm^{-1} cutoff EDGE filter for the 532-nm laser with a 2400 grating and a 1024 pixel deep-depletion CCD. The atomic force microscope was controlled by two piezoelectric drivers, one that controlled the movement of the sample stage in *X*–*Y* and one that controlled the tip in *X*–*Y*–*Z*. The tips were cantilevered tapered glass micropipettes designed for tip-enhanced Raman measurements with a gold nanoparticle placed at the end of the tip. The tip was mounted on a tuning fork. The tuning fork was used to control the distance between the tip and the sample surface. The tip was manually moved to be within several microns of the surface, and the SPM controller moved the tip into contact with the surface using the resonance frequency of the tuning fork for feedback.

Tip-enhanced Raman spectroscopy measurements (near-field) were performed with the laser being focused on the gold tip. For far-field measurements, the tip was retracted approximately 200 nm from the surface and moved laterally out of range by more than 50 microns. The far-field measurements were acquired at the same sample location as the near-field measurements. To obtain new locations on the same sample, the lower piezoelectric driver was used to move the sample to the new position while the tip was out-of-contact with the surface. The location of the tip with respect to the laser was adjusted using continuous Raman acquisitions. Both far-field and near-field measurements were performed at each location.

3 Results and Discussion

Far-field Raman spectra of all samples (carbon-coated silicon and carbon-coated hard disk surface) were first obtained in order to determine the reference state. Figure 2a shows the corresponding far-field measurements for the 20-nm amorphous carbon film while Fig. 2b shows the far-field measurements for the 3-nm carbon overcoat in a hard disk drive. Figure 2c, d shows the corresponding far-field measurements for both samples using a longer acquisition time of 3 min.

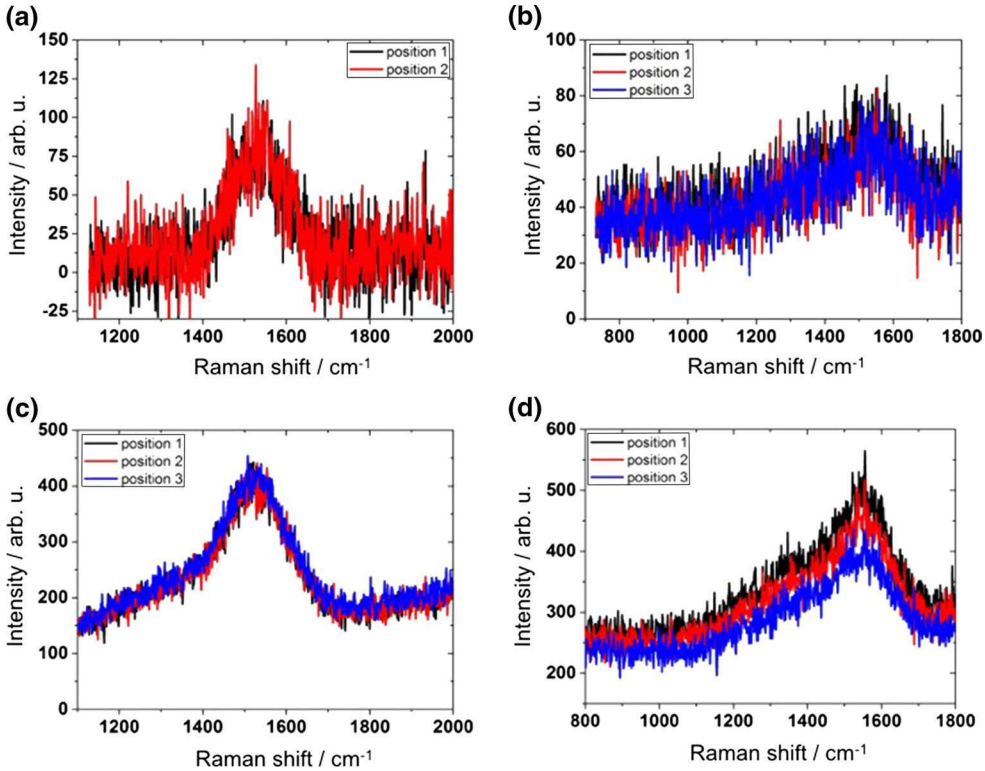

Fig. 2 Far-field Raman spectra for **a** a 20-nm amorphous carbon and **b** a 3-nm carbon overcoat of a hard disk drive measured at different positions. **c** and **d** shows the far-field Raman spectra for a 20-nm amorphous carbon and a 3-nm carbon overcoat of a hard disk drive, respectively, using a longer acquisition time of three minutes

As can be seen in Fig. 2a, b, the spectra for the 20-nm amorphous carbon film and the 3-nm carbon layer of the hard disk drive are similar. Both spectra show a broad Raman peak centered at around 1500 cm^{-1}. The broad Raman peak is typical for amorphous carbon films and is a convolution of the D-peak and G-peak. Line broadening can be correlated with the existing cluster size and the cluster distribution in amorphous carbon films. Moreover, residual stresses in the film due to fabrication can also contribute to a broadened Raman peak [11]. Additionally, it can be observed that both samples give a weak Raman signal with low intensity and poor signal-to-noise ratio. This is because of the small carbon layer thickness of approximately 20 and 3 nm, respectively, and the used experimental conditions, which were necessary to allow a direct comparison between far-field and near-field measurements [12, 13]. Furthermore, the signal-to-noise ratio can be influenced by foreign atoms such as hydrogen or nitrogen incorporated in the carbon network during fabrication [12]. The signal-to-noise ratio and the Raman spectra can be improved by using longer acquisition times. Figure 2c, d shows the far-field Raman spectra of the 20-nm amorphous carbon film and the 3-nm carbon overcoat in a hard disk drive, respectively, measured with an increased acquisition time of 3 min. Similar to Fig. 2a, b, the spectra demonstrate a broad peak centered at around 1500 cm^{-1} (convolution of the D-peak and G-peak) with an increased intensity and improved signal-to-noise ratio. This peak can be deconvoluted and structural information can be gained.

Figure 3 shows a comparison of the far-field and near-field measurements for the amorphous carbon film with a thickness of 20 nm [(a) and (b)] and the 3-nm carbon overcoat of a hard disk [(c) and (d)]. Far-field and near-field spectra were taken at the same position keeping all parameters constant. Two different measurements are shown in order to demonstrate the repeatability of the obtained results.

The far-field spectra for the amorphous carbon film and the carbon overcoat of a hard disk show a weak signal with a broad peak located at approximately 1540 cm^{-1}. On the other hand, the respective near-field measurements show a completely different behavior. In the case of amorphous carbon, two distinct peaks can be observed, located at 1348 and 1605 cm^{-1}, respectively. These peaks can be related to the D-peak and G-peak of typical carbon systems. It is apparent that the near-field spectrum is enhanced compared to the far-field measurement. In addition to these two peaks, a number of additional peaks and shoulders arising at different Raman shift values can be observed. The appearance of these peaks is in good agreement with Veres et al., who studied amorphous carbon films and hydrogenated amorphous carbon films by surface-enhanced Raman spectroscopy. They explained the appearance of those additional peaks by the "composite character" of the D-peak and G-peak. The D-peak and G-peak can be regarded as inhomogeneously broadened bands consisting of a large number of

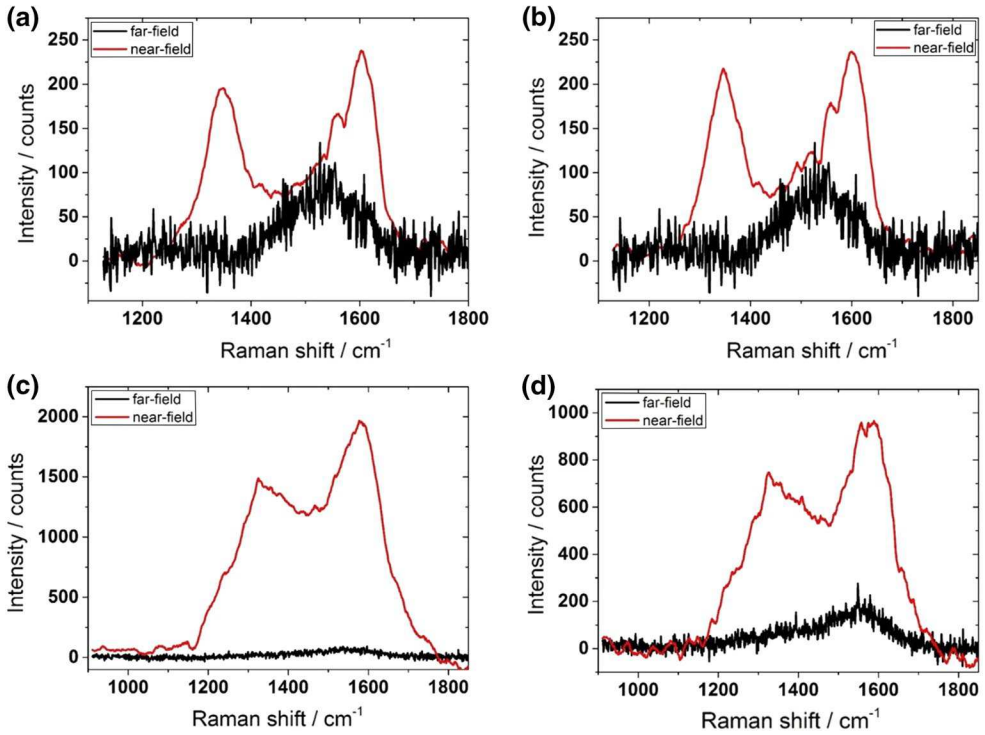

Fig. 3 Near-field Raman spectra for the 20-nm amorphous carbon film (**a**) and (**b**) and the 3-nm-thick carbon overcoat of a commercial hard disk (**c**) and (**d**) obtained at two different positions

individual components. The concentration and Raman cross section of each individual structural unit as well as the distance between the tip and the structural unit determine which unit is selectively enhanced [14]. Kudelski and Pettinger [15] pointed out that the narrow Raman peaks can be traced back to local variations in the carbon configuration. For the 20-nm-thick amorphous carbon film, the maximum enhancement factor for the D-peak and G-peak is about 8 and 3.5, respectively.

In order to calculate the enhancement based upon the enhancement factor, the different spot sizes of the far-field and near-field measurements need to be taken into consideration. This can be calculated using the following equation

$$\mathrm{EF} = C\frac{V_{\mathrm{focus}}}{V_{\mathrm{tip}}}, \tag{1}$$

where V_{focus} represents the volume of the excited far field, V_{tip} represents the volume of the excited field near the tip and C represents the contrast between the far-field and the near-field measurements. Assuming a cylindrical volume field from the laser, we can express Eq. (1) as

$$\mathrm{EF} = C\frac{\pi r_{\mathrm{far}}^2 h_{\mathrm{far}}}{\pi r_{\mathrm{tip}}^2 h_{\mathrm{tip}}}, \tag{2}$$

where r_{far} denotes the radius of the laser spot in the far field, h_{far} represents the height of the far-field focus, r_{tip} represents the radius of the laser sport in the near field and h_{tip} represents the height of the near-field focus. For the far field, r_{far} and h_{far} are about 3 µm and 500 nm, respectively, while for the near field, r_{tip} and h_{tip} are roughly 100 and 20 nm, respectively. Based upon Eq. (2), the enhancement for the D-peak and G-peak in the case of the 20-nm amorphous carbon film can be calculated to be approximately 180×10^3 and 78×10^3, respectively.

In the case of the 3-nm carbon layer of a hard disk, similar experimental results were obtained. The near-field spectra show a significant enhancement with a pronounced D-peak and G-peak at a Raman shift of 1350 and 1582 cm^{-1}, respectively. The maximum enhancement factors are about 47 and 36 for the D-peak and G-peak. This leads to an enhancement by 1057×10^3 for the D-peak and 810×10^3 for the G-peak.

Based upon Fig. 3, it is apparent that the near-field spectra for both samples are enhanced compared to the far-field measurements and that the signal-to-noise ratio is improved. In order to explain these observations, different aspects have to be taken into consideration. The two samples may differ in the degree of amorphicity and the ratio of sp^2–sp^3 hybridization, which can influence the measurements and signal-to-noise ratio. The surface roughness of the 3-nm-thick carbon overcoat of the hard disk drive is expected to

be lower, which can improve the enhancement and reduce the signal-to-noise ratio. The 3-nm carbon overcoat of the hard disk drive is fabricated in a facility dedicated to carbon deposition. Consequently, the influence of foreign atoms on the resulting Raman signal is reduced. In contrast, the sputter facility used for the 20-nm carbon coating is also used for the deposition of various other materials. As a consequence, foreign atoms can play a more pronounced role in reducing possible enhancement as well as affecting the signal-to-noise ratio. Another aspect that needs to be considered is the layout of the individual samples. The 20-nm amorphous carbon film consists of a silicon substrate and a 20-nm amorphous carbon film on the top surface. A hard disk drive typically has a multilayer structure including a lubricant layer on the top surface, followed by a 3-nm carbon overcoat and several other layers magnetic and non-magnetic layers. Some of these layers can contain thin films with platinum group metals and alloys of those metals. Those metals and alloys are normally plasmonically inactive. However, when placing a near-field probe above the surface, the metallic layer may help create a gap mode between the tip and the surface, thereby enhancing the Raman signal [16].

The results presented for amorphous carbon and the hard disk overcoat underline the great advantage of using near-field techniques such as tip-enhanced Raman spectroscopy for the characterization of films with a thickness in the nanometer range. A small carbon layer thickness of 20 or 3 nm can lead to a poor signal-to-noise ratio and rather weak far-field signal. An increase in the acquisition time significantly improves the Raman signal as well as the signal-to-noise ratio. However, longer acquisition times are not recommended since this increases the probability to induce structural changes in thin carbon films by the measurement itself. Due to the signal enhancement in tip-enhanced Raman spectroscopy, materials known as weak Raman scatterers and nanometer-thick films can be investigated with high sensitivity using shorter acquisition times. The increased sensitivity and gain in intensity allow for an accurate deconvolution of the D-peak and G-peak for carbon materials. This in turn enables us to study structural changes such as graphitization and amorphization precisely. Furthermore, the spatial resolution of tip-enhanced Raman spectroscopy is on the order of 50 nm. Due to exact knowledge of the tip location during the measurements, this technique can be used to study induced chemical changes with a high spatial resolution. In heat-assisted magnetic recording, high temperatures, high heating and cooling rates (approx. 10^{11}–10^{12} K/s) and thermal cycling are encountered [17, 18]. This can lead to significant changes of material properties including material degradation and oxidation of the carbon overcoat and the lubricant protecting the magnetic medium [19]. With respect to the carbon overcoat, laser heating may result in oxidation, graphitization, amorphization or a change in the sp^2/sp^3-ratio [17, 20, 21]. Thus, tip-enhanced Raman spectroscopy can serve as a unique characterization technique since it allows the investigation of material changes on a nanometer scale and thereby permits the correlation between a change in materials properties with the tribological performance and reliability of a hard disk drive. Especially for heat-assisted magnetic recording, tip-enhanced Raman spectroscopy can be considered as the right tool due to the accessible scale and high sensitivity, which is needed to successfully probe nanometer-thick carbon films. In order to capture thermally induced changes in the 1.5-nm-thick lubricant layer, it may be necessary to use tip-enhanced IR-spectroscopy.

4 Conclusions

Far-field Raman spectroscopy and tip-enhanced Raman spectroscopy were used to investigate 20-nm-thick amorphous carbon films fabricated by plasma-enhanced chemical vapor deposition and 3-nm-thick carbon overcoats of hard disk drives. From the experimental results, we conclude:

1. The far-field Raman spectrum for both samples was weak and exhibited a poor signal-to-noise ratio due to the small carbon thickness.
2. Near-field spectra were observed for all samples investigated and the recorded near-field Raman spectra demonstrated good repeatability.
3. Significant enhancement using tip-enhanced Raman spectroscopy was observed for all samples tested. The largest enhancement factor was found for the hard disk drive carbon overcoat leading to an enhancement on the order of 10^6.
4. In addition to the well-known D-peak and G-peak for carbon systems, additional peaks arising as shoulders were observed for both samples. The appearance of those peaks is well correlated with published work on similar material systems performed using surface-enhanced Raman spectroscopy.

Based upon the results presented in this paper, it is apparent that tip-enhanced Raman spectroscopy is a promising method for the investigation of thermally induced structural changes in the carbon overcoat of hard disk drives used for heat-assisted magnetic recording.

Acknowledgements Andreas Rosenkranz acknowledges the Feodor Lynen Fellowship of the Alexander von Humboldt foundation. This work was supported by the National Science Foundation (NSF) (Grants CBET-1704085, DMR-1707641, ECCS-1405234 and ECCS-1507146) and the Cymer Corporation. This work was performed in part at the San Diego Nanotechnology Infrastructure (SDNI) of UCSD, a member of the National Nanotechnology Coordinated Infrastructure, which is supported by the NSF (Grant ECCS-1542148).

References

1. Schmid, T., Opilik, L., Blum, C., Zenobi, R.: Nanoscale chemical imaging using tip-enhanced Raman spectroscopy: a critical review. Angew. Chem. Int. Ed. **52**, 5940–5954 (2013)
2. Blum, C., Opilik, L., Atkin, J.M., Braun, K., Kämmer, S.B., Kravstov, V., Kumar, N., Lemeshko, S., Li, J.F., Luszcz, K., Maleki, T., Meixner, A.J., Minne, S., Raschke, M.B., Ren, B., Rogalski, J., Roy, D., Stephanidis, B., Wang, X., Zhang, D., Zhong, J.H., Zenobi, R.: Tip-enhanced Raman spectroscopy—an interlaboratory reproducibility and comparison study. J. Raman Spectrosc. **45**, 22–31 (2014)
3. Stadler, J., Schmid, T., Zenobi, R.: Developments in and practical guidelines for tip-enhanced Raman spectroscopy. Nanoscale **4**, 1856–1870 (2012)
4. Pettinger, B., Schambach, P., Villagomez, C.J., Scott, N.: Tip-enhanced Raman spectroscopy: near-fields acting on a few molecules. Annu. Rev. Phys. Chem. **63**, 379–399 (2012)
5. Berweger, S., Atkin, J.M., Olmon, R.L., Raschke, M.B.: Adiabatic tip-plasmon focusing for nano-Raman spectroscopy. J. Phys. Chem. Lett. **1**, 3427–3432 (2010)
6. Berweger, S., Atkin, J.M., Olmon, R.L., Raschke, M.B.: Light on the tip of a needle: plasmonic nanofocusing for spectroscopy on the nanoscale. J. Phys. Chem. Lett. **3**, 945–952 (2012)
7. Hayazawa, N., Yano, T., Watanabe, H., Inouye, Y., Kawata, S.: Detection of an individual single-wall carbon nanotube by tip-enhanced near-field Raman spectroscopy. Chem. Phys. Lett. **376**, 174–180 (2003)
8. Chen, C., Hayazawa, N., Kawata, S.: A 1.7 nm resolution chemical analysis of carbon nanotubes by tip-enhanced Raman imaging in the ambient. Nat. Commun. **4**, 1–5 (2014)
9. Liao, M., Jiang, S., Hu, C., Zhang, R., Kuang, Y., Zhu, J., Zhang, Y., Dong, Z.: Tip-enhanced Raman spectroscopic imaging of individual Carbon nanotubes with subnanometer resolution. Nano Lett. **16**, 4040–4046 (2016)
10. Saito, Y., Hayazawa, N., Kataura, H., Murakami, T., Tsukagoshi, K., Inouye, Y., Kawata, S.: Polarization measurements in tip-enhanced Raman spectroscopy applied to single-walled carbon nanotubes. Chem. Phys. Lett. **410**, 136–141 (2005)
11. Schwan, J., Ulrich, S., Batori, V., Ehrhardt, H., Silva, S.R.P.: Raman spectroscopy on amorphous carbon films. J. Appl. Phys. **80**, 440–447 (1996)
12. Ferrari, A.C., Robertson, J.: Raman spectroscopy of amorphous, nanostructured, diamond-like carbon, and Nanodiamond. Philos. Trans. R. Soc. Lond. A **362**, 2477–2512 (2004)
13. Chu, P.K., Li, L.: Characterization of amorphous and nanocrystalline carbon films. Mater. Chem. Phys. **96**, 253–277 (2006)
14. Veres, M., Fuele, M., Toth, S., Koos, M., Pocsik, I.: Surface enhanced Raman scattering (SERS) investigation of amorphous carbon. Diam. Relat. Mater. **13**, 1412–1415 (2004)
15. Kudelski, A., Pettinger, B.: SERS on carbon chain segments: monitoring locally surface chemistry. Chem. Phys. Lett. **321**, 356–362 (2000)
16. Katsuyoshi, I., Sato, J., Uosaki, K.: Surface-enhanced scattering at well-defined single crystalline faces of platinum-group metals induced by gap-mode plasmon excitation. J. Photochem. Photobiol. A **221**, 175–180 (2011)
17. Rottmayer, R.E., Barta, S., Buechel, D., Challener, W.A., Hohlfeld, J., Kubota, Y., Li, L., Lu, B., Mihalcea, C., Mountfield, K., Pelhos, K.: Heat-assisted magnetic recording. IEEE Trans. Magn. **42**, 2417–2421 (2006)
18. Kryder, M.H., Gage, E.C., McDaniel, T.W., Challener, W.A., Rottmayer, R.E., Ju, G., Hsia, Y.T., Erden, M.F.: Heat assisted magnetic recording. Proc. IEEE **96**, 1810–1835 (2008)
19. Marchon, B., Guo, X.C., Pathem, B.K., Rose, F., Dai, Q., Feliss, N., Schreck, E., Reiner, J., Mosendz, O., Takano, K., Do, H., Bruns, J., Saito, Y.: Head-disk interface materials issues in heat-assisted magnetic recording. IEEE Trans. Magn. **50**, 3300607 (2014)
20. Pathem, B.K., Guo, X.C., Rose, F., Wang, N., Komvopoulos, K., Schreck, E., Marchon, B.: Carbon overcoat oxidation in heat-assisted magnetic recording. IEEE Trans. Magn. **49**, 3721–3724 (2013)
21. Xu, S., Sinha, S., Rismaniyazdi, E., Wolf, C., Dorsey, P., Knigge, B.: Effect of carbon overcoat on heat-assisted magnetic recording performance. IEEE Trans. Magn. **51**, 3301805 (2015)